nature communications

Article

https://doi.org/10.1038/s41467-026-70165-0

Biomimetic actuator crafted from a relaxor ferroelectric polymer nanocomposite

Received: 17 July 2025

Accepted: 17 February 2026

Hui Chi[1], Peijia Bai[2], Zhengxue Zhou[2], Guangfa Wang[2], Wenhan Xu[3] ✉, Yu Zhang[1], Hao Qin[1], Xinru Wang[1], Yunhe Zhang[1] ✉ & Rujun Ma[2] ✉

Soft actuators have garnered widespread attention due to their distributed actuation and high error tolerance. However, fabricating biomimetic actuators with small-size, simple structure, low energy consumption, and multi-functionality remains challenging. Here, we present a monolayer nanocomposite achieved by incorporating polymer dots into a polyvinylidene fluoride terpolymer. Through interfacial hydrogen bonding and temperature modulation, a gradient distribution of highly polarized regions is achieved within the nanocomposite. This yields ultrahigh electromechanical performance, with an actuation strain of 14.4% and an output mechanical energy density of 1.92 J cm^{-3} at 100 MV m^{-1}. Multifunctional soft actuators are formed from this nanocomposite, weighing only 50 mg, and can skillfully imitate both caterpillar crawling and butterfly flight, unlocking the potential for multimodal locomotion. This insect-sized bionic actuator consumes a mere 3-8 mW. The combination of simple architecture and low energy consumption may pave the way for future development of truly bionic soft robots.

Inspired by the movementsand habits of small creatures in nature, significant efforts have been dedicated in recent years to developing miniature robots[1]. In particular, centimeter-scale robots resembling insects can perform actions such as crawling[2–4], jumping[5–8] and flying[9,10]. Compared with relatively big traditional robots, these insect-sized soft actuators are not only small in size and lightweight, but also have low energy consumption and low cost. The application areas for insect-size soft actuators encompass medical, communications, agricultur,e and military. For instance, they can be precisely maneuvered and deployed in hazardous or hard-to-reach areas, such as scanning for signs of life during search and rescue missions. In forests, swamps, or underground caverns, they can collect environmental data, including temperature, humidit,y and gas composition. Previous studies have described actuators, which can be actuated chemically[11], pneumatically[12], hydraulically, thermally[13,14], or electrically[15,16]. Among these different soft actuators, electrostrictive actuators have shown muscle-like energy density, light weight, flexibility with non-geometric constraints, and fast response[17,18], promising to be designed and manufactured as centimeter-scale crawling or flight robots. However, current insect-sized robots typically have complex transmission structures, which significantly limit their further miniaturization, mechanical robustness, and reduction of energy consumption.

Material selection and design are fundamental to actuation performance[19]. To ensure that insect-size actuators can handle complex terrains and meet diverse operational demands, the ideal actuator material should be capable of performing multiple locomotion modes under electrical stimulation. In addition, current soft robots typically rely on the synergy of multiple material components to ensure smooth operation. Factors such as the flexibility of the passive layers and rigid supporting structures, and the bonding between the distinctive materials, all affect the overall robotic performance. The transmission between the different layers and structures can lead to excessive energy consumption. Bionic soft robots using multifunctional materials are expected to emerge that can integrate actuation and transmission while supporting multiple motion modes.

---

[1]Key Laboratory of High Performance Plastics (Jilin University), Ministry of Education, College of Chemistry, Jilin University, Changchun, China. [2]School of Materials Science and Engineering, Nankai University, Tianjin, China. [3]Deutsches Elektronen-Synchrotron DESY, Notkestr. 85, Hamburg, Germany. ✉e-mail: xuwenhan2015@hotmail.com; zhangyunhe@jlu.edu.cn; malab@nankai.edu.cn

Polyvinylidene fluoride (PVDF) and its various derivatives, including copolymers, terpolymers, and tetrapolymers, have shown promise for electrostrictive actuation[20,21]. However, these relaxor ferroelectric polymers still have limitations, such as much smaller mechanical energy densities compared to piezoelectric ceramics due to inefficient outcoupling of large in-plane expansion in the soft material to generate useful strain and force outputs[22,23].

Herein, we report an all-organic electrostrictive nanocomposite comprised of a relaxor ferroelectric terpolymer P(VDF-TrFE-CFE) and gradiently distributed polymer dots (PDs). The incorporation of CFE monomers into the P(VDF-TrFE) lattice disrupts the long-range ferroelectric order, creating nano-polar regions (PNRs) that are highly responsive to electric fields. This structure is responsible for the high dielectric constant and relaxor ferroelectric behavior of the material, characterized by a large electric-field-induced polarization with minimal hysteresis, which is a fundamental requirement for high-performance electrostrictive actuators. PDs consist of an ordered core and a surface composed of hyperbranched polymer segments rich in sources of hydrogen bonds. Hydrogen bonding formation between the surface functional groups and the fluorine atoms in the terpolymer chains promotes all-trans conformations in the terpolymer. The enhanced interfacial polarization and the increased fraction of polar phase work synergistically to boost the dielectric response and, consequently, the electrostrictive effect. The nanocomposite film exhibits a large actuation strain of 14.4% and an output mechanical energy density of 1.92 J cm^{-3} at 100 MV m^{-1}. Using this nanocomposite film, we fabricated an insect-sized soft motor capable of multiple motion modes. The bionic caterpillar actuator can crawl at a speed of 4.5 cm s^{-1} with an ultra-low input power of only 3.62 mW, an order of magnitude lower than reported crawling devices of comparable size. The biomimetic butterfly actuator flaps its wings at a frequency of 8 Hz, achieving a lift-off height of 2–4 mm, with an input power of 7.98 mW. Both the crawler and butterfly were made solely from this nanocomposite film, without any additional mechanisms to assist in crawling or flying, and the total weight of the actuator is only ~ 50 mg.

Results

Fabrication and interaction mechanism

Fig. 1a shows a schematic of the fabrication process for the relaxor ferroelectric polymer nanocomposite with a gradient distribution of all-trans conformations, which consists of relaxor ferroelectric P(VDF-TrFE-CFE) terpolymers and polymer dots (PDs) (See Method section for details). Briefly, PDs were initially prepared by hydrothermal cross-linking with citric acid and ethylenediamine following the classical bottom-up approach[24]. And PDs were homogeneously mixed with pre-dissolved PVDF terpolymer solution by tip ultrasonic. After that, the solution was drop-casted onto a clean glass and followed by a progressive heating process (60–120 °C) to evaporate the solvent. When the temperature exceeds 60 °C, there is a significant difference in solvent evaporation rates between the upper (in contact with air) and the lower (in contact with a glass substrate) surfaces of the composite film, which results in a higher proportion of all-trans conformations in

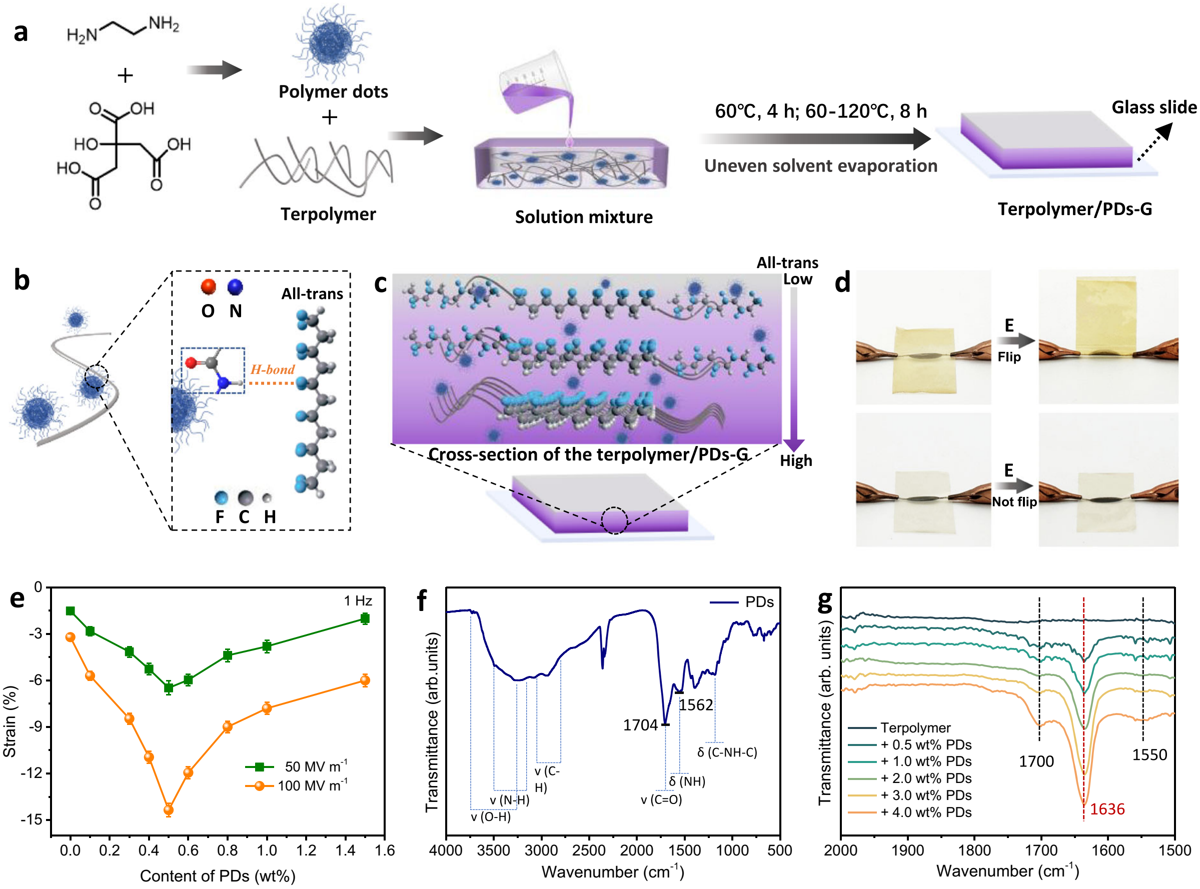

Fig. 1 | Gradient distribution design and hydrogen bonding enhanced all-trans conformations. a Preparation process of the terpolymer/PDs and terpolymer/PDs-G. **b** The interaction mechanism between terpolymers and PDs. (**c**) Cross-sectional view of a composite film with a gradient distribution of all-trans conformation. **d** Comparison of terpolymer-G and the terpolymer/PDs-G before and after application of 42 MV m^{-1} electric field. **e** Actuation strain of P(VDF-TrFE-CFE) with different PDs contents at 50 and 100 MV m^{-1} unipolar fields at 1 Hz. **f** FT-IR spectra of PDs. **g** FT-IR spectra of terpolymers with various contents of PDs. The error bars correspond to the standard deviation of three independent measurements.

the lower layer compared to the upper layer[25]. Note that this optimized composite film is defined as terpolymer/PDs-G, and the pure terpolymer film prepared using a progressive heating process is defined as terpolymer-G. After peeling off the film from the glass substrate, carbon nanotubes (CNTs) dispersion was spray-coated on two surfaces of the polymer film to achieve the elliptically shaped active area as an electrode. By utilizing the abundant functional groups on the PD surface to form hydrogen bonds with the fluorine atoms in the polymer chains, the proportion of all-trans conformations in the composite film is increased (Fig. 1b), resulting in the construction of films with a gradient distribution of all-trans conformations (Fig. 1c). The nanocomposite terpolymer/PDs-G film prepared using this strategy exhibits a giant strain in the presence of an electrical field (Fig. 1d). Under an applied electric field of 42 MV m^{-1}, the terpolymer/PDs-G film folds together directly, while the terpolymer-G film undergoes only minor deformation (Supplementary Movie 1).

Fig. 1e and Supplementary Fig. S1a illustrate the thickness strain (S_3) of nanocomposites with different concentrations of PDs as a function of electric field. As PD content increases, the strain initially rises and then decreases, and the composite with 0.5 wt% PDs content has the highest strain. This is due to the best hydrogen bonding interactions between PDs and the terpolymer in the 0.5 wt% PDs doped composites. To assess the robustness and standardization potential of our gradual-heating process, we rigorously evaluated its batch-to-batch reproducibility. Multiple independent batches of the terpolymer/PDs-G (c_{PDs}=0.5 wt%) composite were fabricated under identical conditions. The electrostrictive strain values of these new batches were highly consistent with the data from our original batch reported above (Supplementary Fig. S2). The exceptionally low standard deviations relative to the mean values confirm that our fabrication process is stable, straightforward to standardize, and yields highly reproducible, high-performance materials. To analyze the reason for the superior performance of the gradient-distributed structure composite, we investigated the effect of PDs introduction and the impact of the gradient structure on the performance of the nanocomposites using the control variable approach, respectively. First, to study the influence of PDs on the composite from a microscopic perspective, we prepared uniformly distributed composite films (named as terpolymer/PDs) and terpolymer films by the slow solvent evaporation method at a constant temperature of 60 °C. The Fourier transform infrared (FT-IR) spectrum of PDs (Fig. 1f) confirms the presence of amide functional groups, as evidenced by their vibrational fingerprints centered at 1562 cm^{-1} (N-H in-plane bending), 1704 cm^{-1} (C=O stretching of the amide bond), and 3300 cm^{-1} (N-H stretching). As shown in Fig. 1g, after incorporating PDs into the terpolymer, the bending absorption peak of the N-H (in-plane bending) shifted to 1550 cm^{-1}, and a very obvious absorption peak appeared at 1636 cm^{-1} which increased with the increase of PDs content. This phenomenon is attributed to the formation of hydrogen bonds between the N-H of the amide bond in the PDs and the fluorine atom in the terpolymers[26], and hydrogen bonds can induce the formation of all-trans conformation in PVDF-based polymers[27]. The gradient distribution of the all-trans conformation, rather than the spatial distribution of PDs, is the primary outcome of our gradual-heating process. While the PDs are uniformly dispersed due to good compatibility with the terpolymer matrix, the thermal gradient during film formation creates a corresponding solvent evaporation rate gradient. The bottom surface of the film, experiencing a slower evaporation rate, facilitates a more orderly arrangement of polymer chains into the all-trans conformation. The PDs, rich in hydrogen-bonding sites, locally amplify this effect by stabilizing the all-trans conformation around them. Thus, the driving force is the evaporation rate gradient templated by the thermal gradient, which directly programs the gradient in polymer chain conformation.

X-ray diffraction (XRD) pattern shows the (110/200) reflection of composites shifting towards higher angles (Fig. 2a). This indicates that the introduction of PDs reduced the interchain spacing of the terpolymer. By comparing FT-IR spectra, we observed an increase in the all-trans conformation within the terpolymer following the introduction of PDs (Fig. 2b). To visualize the polar network in the nanocomposite more directly, we performed atomic force microscopy-infrared spectroscopy (AFM-IR) on both the terpolymer and the nanocomposite[28]. In the chemical image of the terpolymer/PDs, the polar network structure was clearly visible (Fig. 2c), whereas the terpolymer lacked a polar network due to the absence of the all-trans conformation (Fig. 2d). Local infrared spectroscopy confirmed that PDs introduction indeed induces the formation of the all-trans conformation in the terpolymer (Fig. 2e and 2f). In contrast, due to all-trans conformation defects, homogeneous chemical mapping existed for the terpolymer (Fig. 2d). The thermal properties of the composites with varying PDs contents were characterized by differential scanning calorimetry (DSC). The second heating cycle revealed that both the melting temperature and melting enthalpy of the composite films exhibited a gradual decrease with increasing PDs content (Supplementary Fig. S3). This trend indicates that the incorporation of PDs, through hydrogen bonding, significantly influences the microstructure of the polymer matrix, likely by altering the chain packing and organization associated with the all-trans conformation. We measured the S_3 of these uniformly distributed all-trans conformation films (Supplementary Fig. S4 and S5), which were 5.6% (10 Hz) and 6.7% (1 Hz) for terpolymer/PDs and 2.5% (10 Hz) and 3.1% (1 Hz) for the pure terpolymer at 100 MV m^{-1}. The electrostrictive performance of composites was significantly enhanced by introducing PDs. The electrostrictive strain was characterized at 1 Hz and 10 Hz to ensure direct comparability with established literature and to assess the frequency-dependent response[20,21]. The marginally higher strain at 1 Hz is typical of relaxor ferroelectrics, reflecting the enhanced polarization alignment at lower frequencies. The maintained performance at 10 Hz confirms the material's capability for faster actuation, highlighting its versatility across different operational regimes. It is noteworthy that the absolute electromechanical performance of P(VDF-TrFE-CFE) can be influenced by several intrinsic and extrinsic factors, including the specific monomer ratio and film-processing history. Therefore, the most critical and rigorous assessment of any enhancement strategy is a direct comparison against a control sample prepared and characterized under identical conditions, as performed in this work. All strain data reported herein were derived from multiple parallel measurements, with error bars confirming the high reproducibility of our results. We obtained the polarization response for the terpolymers and nanocomposites under unipolar and triangular electric fields (Supplementary Fig. S6 and S7), and the slender hysteresis loops showed the relaxor ferroelectric properties of the terpolymer/PDs. The composites exhibited higher polarization than that of pure terpolymers under electric fields, and the terpolymer/PDs displayed higher polarization of 0.064 C m^{-2} than the terpolymer of 0.057 C m^{-2} under an electric field of 100 MV m^{-1} at 1 Hz.

Effect of polymer films with a gradient distribution of all-trans conformation on actuation strain

After clarifying the interaction between PDs and terpolymers, we analyzed the mesoscopic structure of the films with a gradient of all-trans conformation. The FT-IR spectra of the upper and lower surfaces of the terpolymer films before and after the introduction of PDs confirmed that all-trans conformations were concentrated on one side (Fig. 3a). The absorption peak intensity of the lower surface of the composite at 1286 cm^{-1} was significantly higher than that on the upper surface of the composite, whereas the absorption peak intensity of the lower surface of the terpolymer at 1286 cm^{-1} was slightly increased

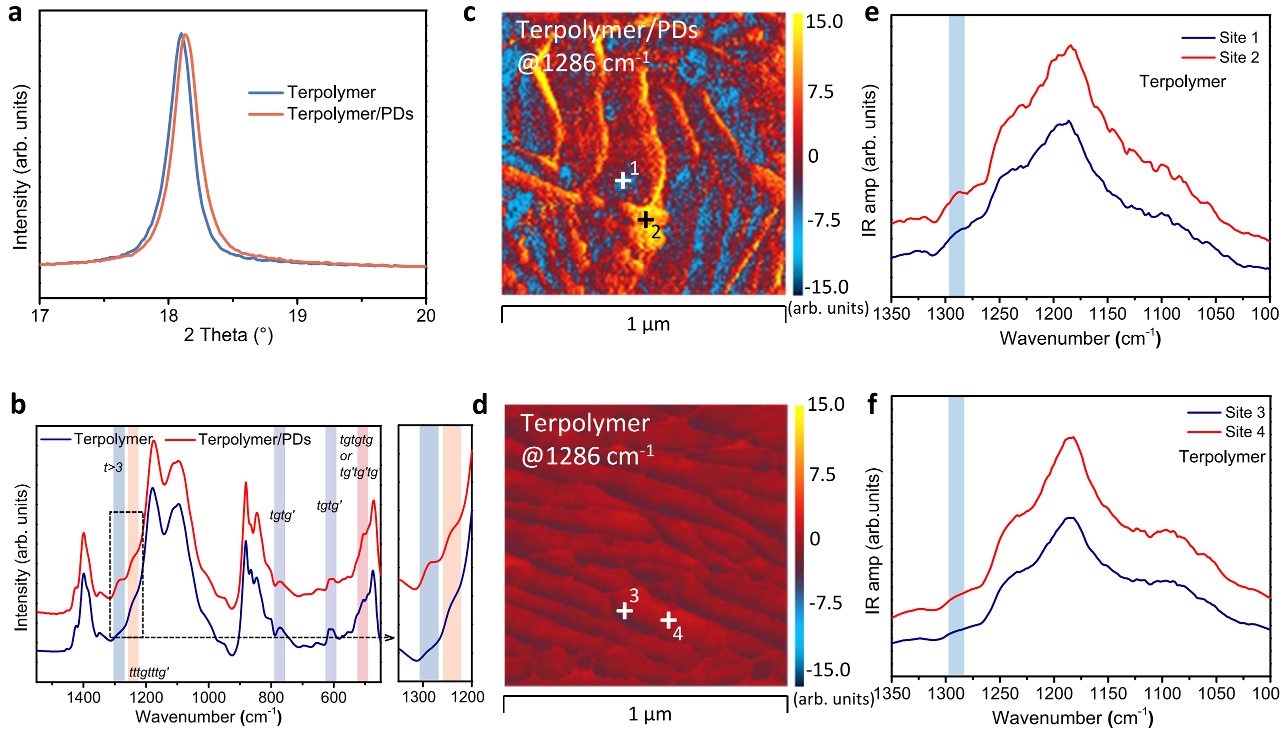

Fig. 2 | Structural analysis of terpolymer and terpolymer/PDs composite films with uniform distribution of all-trans conformations. **a** X-ray diffraction patterns of terpolymer and terpolymer/PDs nanocomposite (c_{PDs} = 0.5 wt%). **b** FT-IR spectra of terpolymers with various contents of PDs. AFM-IR characterization of the polar phase distribution in (**c**) the terpolymer/PDs nanocomposite (c_{PDs} = 0.5 wt%) and (**d**) terpolymer. Local IR spectra of the marked positions for (**e**) the terpolymer/PDs nanocomposite (c_{PDs} = 0.5 wt%) and (**f**) the terpolymer.

compared to that on the upper surface. Fig. 3b shows the grazing incidence XRD patterns of the upper and lower surfaces of terpolymers and terpolymer/PDs composites. The reflection of the lower surface of the polymer film before and after adding PDs was shifted towards a higher angle compared to the upper surface, indicating a decrease in the interchain spacing between the lower surfaces of the terpolymer and composites. The introduction of PDs increases the number of all-trans conformations, while gradual heating promotes the uneven distribution of these increased all-trans conformations.

The spatial chemical analysis of the cross-sections of terpolymer-G and terpolymer/PDs-G based on AFM-IR was shown in Fig. 3c-f (laser irradiation frequency of 1286 cm^{-1}, corresponding to all-trans conformation). Five points were selected from bottom to top on the cross-section of the materials, and local infrared spectroscopy confirmed that the cross-section of the terpolymer/PDs-G gradually decreased in all-trans conformation from bottom to top (Fig. 3e), with a slow change process rather than a sudden change. The local infrared spectrum of the cross-section of the terpolymer-G was shown in Fig. 3f, and the all-trans conformation also changed slowly. The interconnection network of polar phases can be clearly seen in the chemical image of the terpolymer/PDs-G composite (Fig. 3c). On the contrary, owing to the deficiency of all-trans conformation, homogeneous chemical mapping was present in the terpolymer (Fig. 3d). The AFM-IR of the upper and lower surfaces of the terpolymer-G films before and after the introduction of PDs more intuitively confirmed the phenomenon of concentrated distribution of all-trans conformation on one side (Supplementary Fig. S8). The polar phase was most pronounced on the lower surface of the composite film by laser irradiation at 1286 cm^{-1}. We performed high-resolution transmission electron microscopy (HRTEM) on the upper and lower layers of the cross-section of the terpolymer/PDs-G composite (Fig. 3g, 3j). The fast Fourier transform indicated that the terpolymer at the interface between the lower layer of terpolymer/PDs-G (Fig. 3h) exhibited more all-trans conformation than the upper layer (Fig. 3i). We compare the actuation strain of all-trans conformational changes originating from enhanced hydrogen bonding interactions in a gradient-distributed structure. Fig. 3k, S1b, and S9 show the S_3 of terpolymer/PDs-G under different electric field strengths. At 100 MV m^{-1}, the S_3 of the terpolymer/PDs-G film reaches 13.1% at 10 Hz and 14.4% at 1 Hz, whereas that of the terpolymer-G film is only 3.0% at 10 Hz and 3.2% at 1 Hz, which is an improvement of approximately 330 - 350%. As shown in Fig. 3l, the terpolymer/PDs-G film exhibits the largest actuation performance when compared to inorganic, organic, and composite materials reported in the literature[20,22,29–32]. In addition, as the frequency increases, the peak of the dielectric constant (ε_r) of the terpolymer/PDs-G film shifts to higher temperatures, indicating its relaxor ferroelectric properties (Supplementary Fig. S10). 0.5 wt% of terpolymer/PDs-G shows a higher ε_r than that of terpolymer-G at 1000 Hz and room temperature, which contributes to the enhancement of its electrostrictive performance (Supplementary Fig. S11). Meanwhile, the P-E loops of the terpolymer-G and terpolymer/PDs-G nanocomposites under unipolar and bipolar electric fields (Supplementary Figs. S12 and S13) display slim hysteresis curves, further confirming their relaxor ferroelectric behavior. Moreover, under an electric field of 100 MV m^{-1} and a frequency of 1 Hz, the polarization of the composite material reaches 0.070 C m^{-2}, which is higher than 0.059 C m^{-2} for terpolymer-G.

Electrostriction coefficient (Q_{33}) is a key parameter for evaluating the electrostriction properties of materials. Based on the electrostrictive strains (Fig. 3k and Supplementary Fig. S1b) and polarizations (Supplementary Fig. S12), we derived the Q_{33} of nanocomposites and pristine terpolymer under different electric fields (Supplementary Fig. S14) from the equation: $S_3 = Q_{33}P^2$. Q_{33} of terpolymer/PDs-G is more than twice as much as that of the terpolymer-G. At 100 MV m^{-1} and 1 Hz, the $|Q_{33}|$ of terpolymer/PDs-G

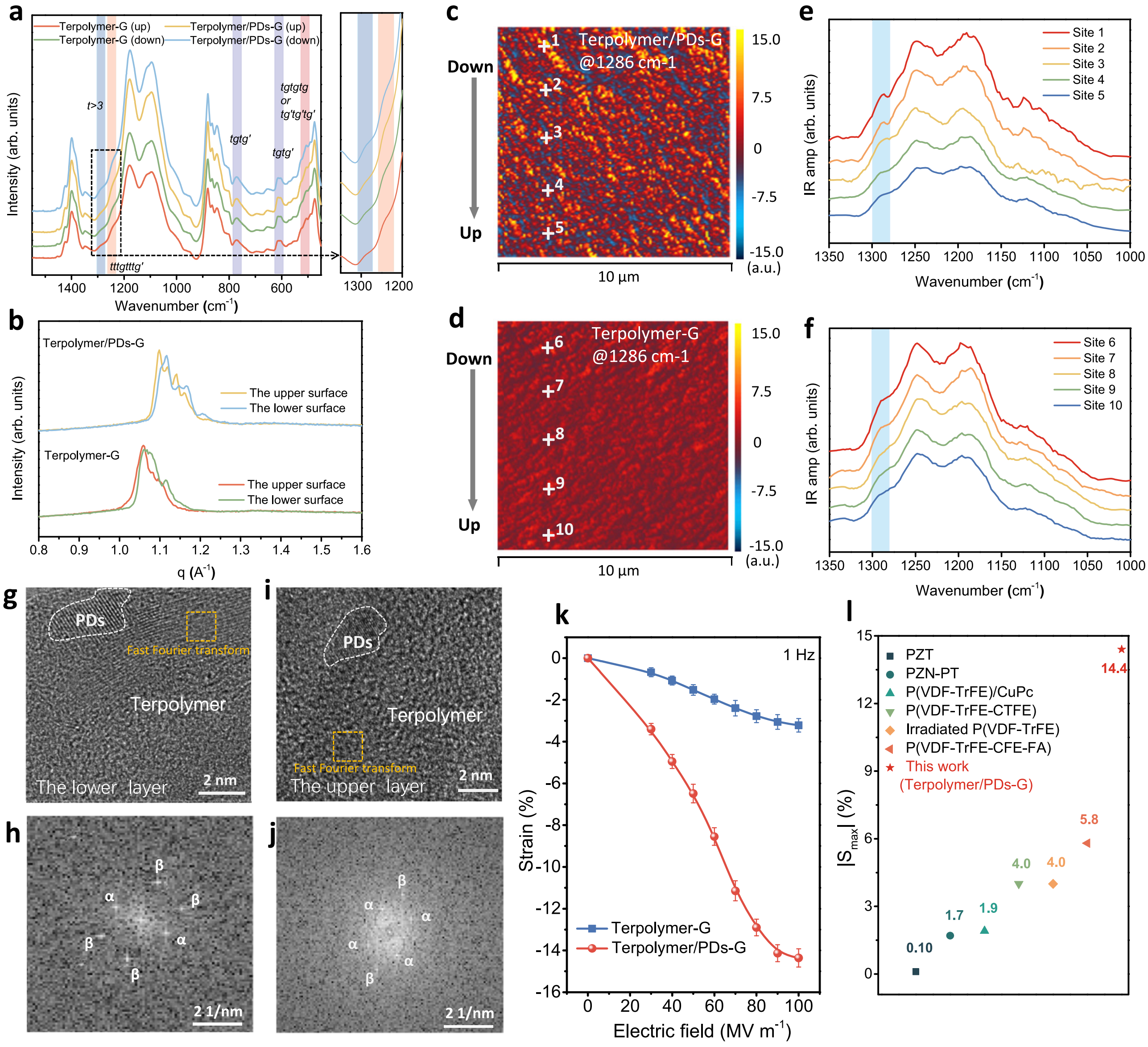

Fig. 3 | Structural analysis and Electrostriction performance of terpolymers and terpolymer/PDs composite films with gradient distribution of all-trans conformations. **a** FT-IR spectra of the upper and the lower surfaces for terpolymer-G and the terpolymer/PDs-G nanocomposite ($c_{PDs} = 0.5$ wt%). **b** XRD patterns of the upper and the lower surfaces for terpolymer-G and the terpolymer/PDs-G nanocomposite ($c_{PDs} = 0.5$ wt%). AFM-IR characterization of the polar phase distribution in (**c**) the terpolymer/PDs-G nanocomposite ($c_{PDs} = 0.5$ wt%) and (**d**) terpolymer-G. Local IR spectra of the marked positions for (**e**) the terpolymer/PDs-G nanocomposite ($c_{PDs} = 0.5$ wt%) and (**f**) terpolymer-G. HRTEM images of **g** the lower and **i** the upper layer of the terpolymer/PDs-G nanocomposite ($c_{PDs} = 0.5$ wt%). Fast Fourier transform of the selected region in (**h**) **g** and (**j**) in **i**. **k** Actuation strain of terpolymer-G and the terpolymer/PDs-G nanocomposite ($c_{PDs} = 0.5$ wt%) at 1 Hz unipolar field versus electric field. **l** Comparison of the electromechanical performance of various materials in terms of the maximum strain $|S_{max}|$. P(VDF-TrFE-CFE-FA), where FA denotes fluorinated alkyne[20]; P(VDF-TrFE-CTFE), where CTFE denotes chlorotrifluoroethylene[29]; irradiated P(VDF-TrFE)[30]; P(VDF-TrFE)/CuPc[31]; PZN-PT[22]; PZT[32]. The error bars correspond to the standard deviation of three independent measurements.

is 44.3 m^4 C^{-2} while that of terpolymer-G is only 10.6 m^4 C^{-2}. The electromechanical coupling factor (k_{33}) can be calculated from output mechanical energy with $k_{33} = \sqrt{\frac{\text{output mechanical energy}}{\text{input energy}}}$[33]. At 100 MV m^{-1} and 1 Hz, the k_{33} of terpolymer/PDs-G is 0.370 while that of terpolymer-G is 0.0794 (as shown in Supplementary Fig. S15). For effective operation of electric actuators, the driving material must have excellent mechanical energy density (E_m) to generate sufficient force to move the load. Mechanical energy density is defined as $E_m = 0.5YS^2$ (Y, elastic modulus; S, actuation strain). The large strain and modulus (0.186 GPa) in the terpolymer/PDs-G produced 1.92 J cm^{-3} (Supplementary Fig. S16), which is nearly twice that of ferroelectric polymers and polymer composites, and even comparable to ferroelectric ceramics.

To investigate whether the deformation effect of protrusion or depression in composites is related to the elastic modulus of the upper and lower surfaces, we measured the elastic modulus of the upper and lower surfaces of the films with a relatively uniform distribution of all-trans conformation before and after adding PDs (Supplementary Fig. S17). The elastic moduli of the composites were generally higher than those of the terpolymers, with the elastic moduli of the upper and lower surfaces of the terpolymer being 153 MPa and 156 MPa, respectively, while those of the terpolymer/PDs were 170 MPa and 175 MPa for the upper and lower surfaces of the terpolymer/PDs, respectively. The elastic modulus of the materials with a uniform distribution of the all-trans conformations was slightly higher for their lower surfaces than for their upper surfaces. Supplementary Fig. S18 showed the elastic modulus of the upper and lower surfaces of films with all-trans conformation gradient distribution before and after the addition of PDs. The elastic moduli of the upper and lower surfaces of the terpolymer-G were 163 MPa and 167 MPa, respectively, while the elastic moduli of the upper and lower surfaces of the terpolymer/PDs-G composites were 183 MPa and 189 MPa, respectively. The differences in elastic modulus between the upper and lower surfaces of the two were similar to those of terpolymers and composites with a uniform distribution of all-trans conformation. The composites with a gradient distribution of all-trans conformation can realize unidirectional bending actuation. Therefore, the deformation effect of composites that can achieve protrusion or depression was mainly related to the gradient distribution of all-trans conformation, but not to the elastic modulus of the upper and lower surfaces. This asymmetry between the upper and lower surfaces caused the polymer composite to form a structure similar to that of a classic unimorph device, allowing the single-layer polymer film to bend under an electric field. Leveraging this unique characteristic, we have developed a complete caterpillars-to-butterflies biomimetic robotic system.

The manufacture and performance of the caterpillars-to-butterflies bionic actuation system

Nanocomposites with a gradient structure have excellent actuation properties because they form a natural single deformation. The actuator made of this nanocomposite has the potential to create insect-size robots. The breakdown strength of terpolymers and nanocomposites is shown in Supplementary Fig. S20. The introduction of PDs increases the breakdown strength by about 27 MV m^{-1} to 249 MV m^{-1}. To gain deeper insight into the mechanism behind the enhanced dielectric breakdown strength, we employed thermal-stimulated depolarization current (TSDC) and leakage current measurements (Supplementary Fig. S21 and S22). The TSDC spectrum of the terpolymer/PDs-G composite revealed a main relaxation peak shifted to a higher temperature (24.9 °C) compared to that of the pure terpolymer-G (23.8 °C), indicating the presence of deepened energy traps for charge carriers, which we attribute to the strong hydrogen-bonded interfaces. Furthermore, the composite exhibited a lower leakage current density than the pure polymer under high electric fields (Supplementary Fig. S22). These findings collectively demonstrate that the PDs, via hydrogen bonding, create effective charge traps that suppress charge injection and transport. This suppressed conduction is a key factor in delaying the onset of dielectric breakdown, thereby contributing to the breakdown strength and reliability of the composite. When fabricating dielectric devices, breakdown strength is a critical material property metric, requiring that the applied electric field remain below 20% of the breakdown strength[20]. For actuators fabricated from our materials, actuation performance at an electric field below 50 MV m^{-1} is particularly crucial.

The upper surface of the terpolymer/PDs-G was placed upward, as shown in Fig. 4a. The composite was made into a shape similar to that of a caterpillar. The head and tail of the caterpillar are sharper and narrower compared to the abdomen. A slightly wider abdomen provides sufficient power while crawling, and the head and tail are designed with symmetrical circular arcs to reduce the resistance of the caterpillar to extend and stretch its body during the crawling process. The electrode coating is applied in the middle of the material, and the elliptical electrode was designed to ensure the stable crawling of the caterpillar during the crawling process. The crawling route is designed as a bumpy ladder structure, which is more in line with the various complex road conditions encountered by caterpillars during their survival in nature. Supplementary Fig. S19a shows the complete morphology of the crawling device. In the presence of an electric field, the caterpillars can steadily crawl at a peristaltic frequency of 2 Hz. The caterpillar crawled a distance of 9 cm in 2 s, with a crawling speed of up to 4.5 cm s^{-1}. The operating voltage and current are shown in Supplementary Fig. S23, and the single-cycle energy consumption can be calculated ($W = UIt$, U, single-cycle voltage; I, single-cycle current; t, single-cycle elapsed time). The single-cycle energy consumption is only 9.04×10^{-4} J. We recorded the crawling process using a high-speed camera (Fig. 4b, Supplementary Movie 2).

In contrast to the above process, by changing the shape of the film and control conditions, going through such a cocooning process, we also produced a bionic butterfly flight actuator from this material. As shown in Fig. 4a, the composite was made to resemble the shape of a butterfly. The head and tail of the butterfly were designed in a streamlined shape. The reason for the small, curved, streamlined shape of the head is that it carries the head of the butterfly when the wings swing upward. Then, when the wings were swung downward, the large, curved, streamlined shape of the tail was designed to allow the butterfly to take off from the ground. We coated the electrodes in the middle area of the material and designed the electrode area in an elliptical shape because the elliptical active area was more conducive to driving the wings on both sides. In the presence of an electric field, the wings achieved reversible flapping behavior. The operating voltage and current are shown in Supplementary Fig. S24, and single-cycle energy consumption was only 4.99×10^{-4} J. Supplementary Fig. S25a shows the complete morphology of the flight device. We recorded the actuation process using a high-speed camera (Fig. 4c, Supplementary Movies 3 and 4). Without any additional auxiliary equipment, the active actuation area in the center of the film alone can carry up to 20 times its own weight, allowing the flight device to reach a height of 2-4 mm above the ground. To precisely evaluate its actuation performance, we systematically characterized the variation of the angular displacement of the butterfly wing with the applied electric field. We systematically characterized the angular displacement of the butterfly wing as a function of the applied electric field (Supplementary Fig. S26). As shown in Supplementary Movie 5, the actuator demonstrates rapid, reversible, and highly repeatable flapping behavior under a 1 Hz electric field. The flipping angle of the wing steadily increases with the electric field strength. Quantitative data reveal that the angular displacement grows from a slight movement at low fields to a substantial angle of approximately 90° at an electric field of 50 MV m^{-1}. This significant angular displacement not only visually confirms the success of our gradient design in amplifying local high strain into effective macroscopic motion but also signifies that this all-organic actuator has reached a state-of-the-art level in its output capability.

The two insect-sized actuators are lightweight. The bionic caterpillar actuator weighs 55.4 m,g and the bionic butterfly actuator weighs 44.8 mg. As shown in the Table S1, both actuators are significantly lighter than those reported in existing studies[3,17,34–40], demonstrating a substantial weight advantage for their class. To quantitatively evaluate the energy efficiency of our actuators, we calculated the input power per cycle from the recorded voltage and current transients during operation, defined as $P = W/t$ (W, single-cycle energy consumption; t, single-cycle elapsed time). The most rigorous validation of our material strategy comes from a direct comparison under identical actuator designs. We fabricated bio-inspired caterpillars and butterflies using both the terpolymer/PDs-G composite and the control terpolymer-G. Remarkably, to achieve a comparable actuation strain, the terpolymer/PDs-G actuator requires a driving field of only 30 MV m^{-1}, whereas the terpolymer-G actuator necessitates 100 MV m^{-1} (Fig. 3k). Their operating voltage and current are shown in Supplementary Figs. S27 and S28, and their motion behavior is depicted in Supplementary Movies 6 and 7. This drastic reduction in the required operating field directly translates to a substantial decrease in input power. Specifically, the input power for the terpolymer/PDs-G caterpillar actuator is 2.532 mW, which is an order of magnitude lower than the 26.32 mW required by the terpolymer-G caterpillar at their respective driving fields. A similar power reduction was confirmed for the butterfly actuators (5.248 mW vs. 57.94 mW). This internal comparison provides definitive evidence that our composite material enables ultra-

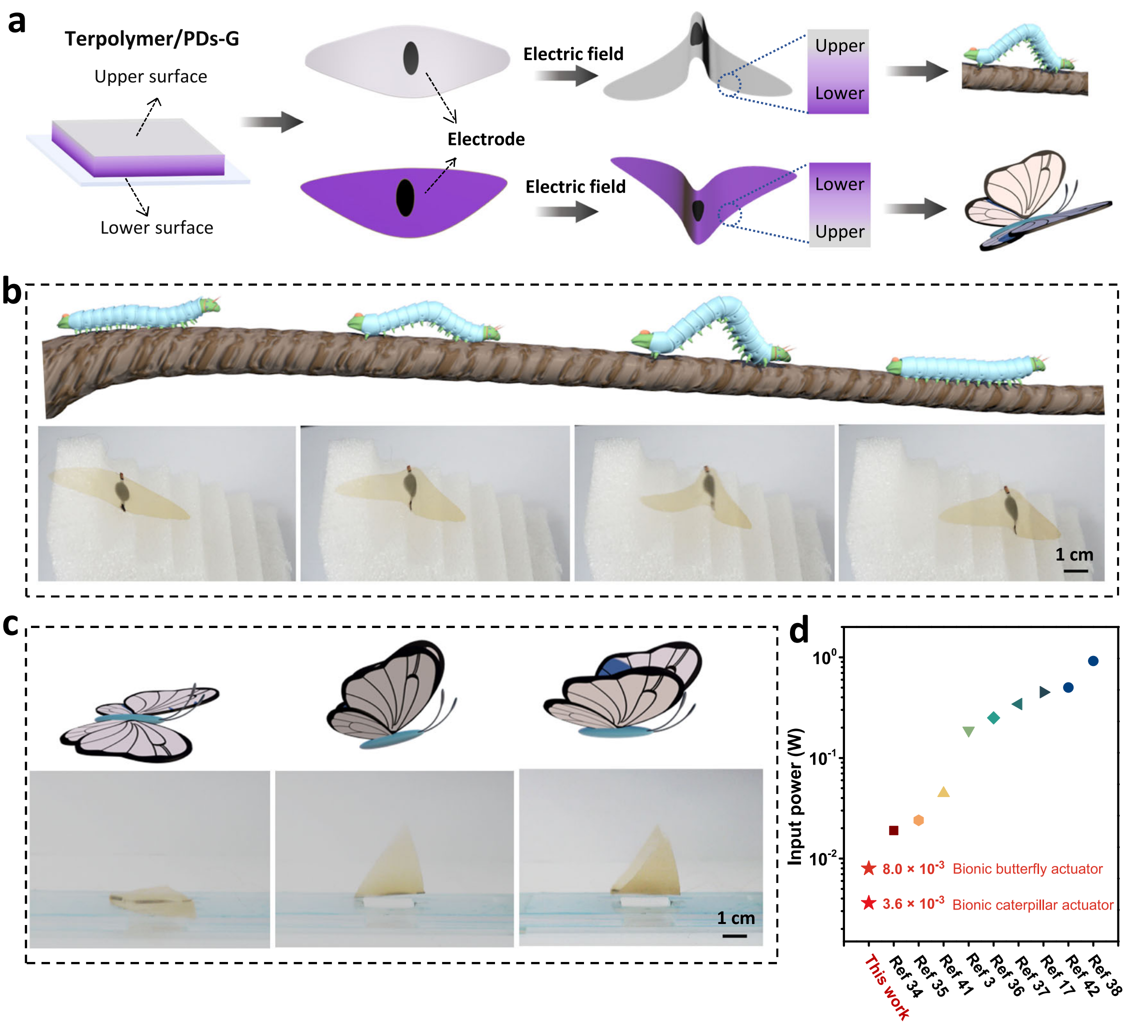

Fig. 4 | Actuation mechanism of caterpillars-to-butterflies bionic system. **a** Schematic illustrating the crawling mechanism of a bionic caterpillar actuator and the flight mechanism of a bionic butterfly actuator. **b** The crawling process of the bionic caterpillar actuator and **c** the take-off process of the bionic butterfly actuator under time-lapse photography. **d** Comparison of input power of two actuators in this work with other works in literature[3,17,34–38,41,42]. The applied electric field of the above actuators is 42 MV m^{-1}.

low power consumption. Furthermore, compared with other reported electric soft actuators (Fig. 4d, Table S1)[3,17,34–38,41,42], our terpolymer/PDs-G actuators (consuming 3.62 mW and 7.98 mW at higher performance regimes) also demonstrate highly competitive, low input power, underscoring their overall efficiency and practical potential. The achievement of two locomotion modes using a single material with ultra-low energy consumption allows for a targeted approach to meet different needs, which is unprecedented. The composite has enormous application value in the field of soft robot actuation and provides ideas for the profound development of sensors.

While this work demonstrates that our single-layer, gradient composite actuator achieves exceptional performance in terms of strain, low mass (~50 mg), and ultra-low input power (on the order of milliwatts), we acknowledge that its current operational framework requires a high driving voltage (~1.5 kV). This requirement for an external high-voltage source presents a recognized challenge for the development of fully untethered, autonomous soft robots, as it necessitates ancillary power conversion circuitry. The core trade-off in our present design is indeed the achievement of a simplified, monolithic fabrication process and high electromechanical performance at the cost of operational voltage. However, it is crucial to distinguish between operating voltage and input power. The low power claim central to this work refers to the minimal energy consumption (in mW) during operation, a metric in which our actuators are highly competitive, as benchmarked in Table S1. This low power consumption, combined with the exceptionally low mass of the active material itself, is a critical step toward future energy-autonomous systems. The single-material, unimorph architecture eliminates interfacial energy losses common in multi-layer laminates and is the direct cause of the low mass and simple structure that enable complex biomimetic motions. Future work will squarely focus on overcoming the voltage limitation, through strategies such as developing much thinner films or exploring multi-layer co-fabrication to reduce the required driving voltage to more practical levels without compromising the achieved benefits of low mass and power.

Discusssion

The relaxor ferroelectric nanocomposite exhibits high actuation strain, mechanical energy density, and electromechanical coupling factor. These properties are attributed to the unique gradient structure of the composite, which enables unimorph-like behavior. A special temperature modulation process results in a gradient distribution of the all-trans conformation within the composite film. The nanocomposite film exhibits a large actuation strain of 14.4% and an output mechanical energy density of 1.92 J cm^{-3} at 100 MV m^{-1}. A thin-film actuator based on this high-strain composite and having an elliptical active area reproduces the motion patterns of both caterpillars and butterflies. The bio-inspired caterpillar crawling actuator can stably crawl at a speed of 4.5 cm s^{-1} under 42 MV m^{-1} and 2 Hz, while the butterfly-inspired flying actuator can lift its wings 2–4 mm off the ground at 8 Hz and 42 MV m^{-1}. The effective electrode area can support up to 2000% of its own weight. These lightweight, low-energy, and multi-mode actuators provide a scalable approach for the development of insect-size robots.

Methods

Materials

P(VDF-TrFE-CFE) terpolymer with the composition of VDF/TrFE/CFE = 61.2/31.3/7.5 mol% was obtained from Piezo Technologies, France. N,N-dimethylformamide (DMF) was purchased from Sigma-Aldrich. Citric acid (CA) was obtained from Aladdin, and ethylenediamine (EDA) was received from Sinopharm Chemical Reagent co., Ltd. All the chemicals were used as received.

Synthesis of polymer dots

In this work, the PDs were prepared following a classical bottom-up method, hydrothermal crosslinking[24], as shown in the Supplementary Fig. S29. CA (1.0507 g) and EDA (335 μL) were initially dissolved in deionized water (10 mL). Then the mixed solution was transferred to a poly(tetrafluoroethylene) (Teflon)-lined autoclave (30 mL) and heated at 180 °C for 7 h, the reactors were naturally cooled to room temperature. At the end of the reaction, the solution was transferred to a dialysis bag for 30 h. After dialysis, the solution was freeze-dried for 72 h to obtain brown PDs. Finally, the brown-black powders PDs were obtained (Supplementary Figs. S30–S32, Supplementary Information for relevant characterization of PDs).

Polymer/polymer dots (PDs) composite films preparation

In the preparation of the composite films (terpolymer/PDs-G) shown in Supplementary Fig. S33, 0.3 g of terpolymer was dissolved in 5 mL DMF and stirred overnight at room temperature. Depending on the required mass fraction in the composites, the appropriate weight of PDs was dissolved in 3 mL of DMF and sonicated for 1 h before using. These homogeneous solutions were then dropped onto a 6 cm × 6 cm clean glass slide and placed in an oven at 60 °C for 4 h, then the temperature was slowly raised to 120 °C within 8 h. Afterward, the polymer films were placed in a vacuum oven and annealed at 120 °C for 12 h (corresponding to a controlled ramp rate of 7.5 °C h^{-1}). The thickness of the films was in the range of 30 μm to 40 μm. The distribution of characteristic elements in terpolymers and composites was characterized by energy dispersive X-ray spectroscopy (EDS), as shown in Supplementary Fig. S32. The appearance of the O element in the EDS image of the composite indicates the successful introduction of PDs into the terpolymer, and the uniform distribution of elements suggests the uniformity of the composites. The terpolymer/PDs films with uniformly distributed all-trans conformation were treated at 60-120 °C for 12 h during the preparation process to evaporate the solvent, and the other treatment methods were the same as the above process for terpolymer/PDs-G.

The fabrication and construction of the bionic caterpillar crawling actuator and the bionic butterfly flight actuator

The prepared polymer composite film was cut into homogeneous texture according to the shape and size as shown in Supplementary Figs. S34 and S35 and carbon nanotubes (CNT, XFNANO, purity > 90%, 1–2 nm in diameter and 1–3 μm in length) were deposited on the surface of the composite film by spray-coating (Dahua, DH350E) to form the elliptical shaped active area as electrodes, and the active area was extended to the upper and lower edges of the film through elongated conductive regions, respectively. The ultra-thin copper strips (0.06 mm in thickness) were attached onto the composite film with conductive adhesive to serve as a skeleton support, and connected to the high-voltage power supply through ultrafine copper wires (0.03 mm in diameter). In the bionic caterpillar crawling actuator, we designed the crawling route as a stepped structure with a slope of 40° and a length of 90 mm to simulate the rough tree-like structure in nature. Specific details can be seen in Supplementary Fig. S19, Supplementary Movie 2. For the bionic butterfly flight actuator, in order to avoid the impact of the force generated by the wings flapping on the ground on the mechanical and electrical performance display of the composites, all flight tests were conducted on narrow glass platforms, with a 1 cm small square set in the center of the glass platform to slightly sink the active area of the flight actuator, allowing the wings to be upwardly folded (Supplementary Fig. S25 and Supplementary Movies 3 and 4).

Characterizations and measurements

The SEM experiment was captured on a JEOL JSM-7401F scanning electron microscope with an EDS analysis attachment. The TEM and HRTEM images were obtained by a JEM-2100F instrument. The films were embedded in epoxy resin and then sectioned using an EM UC7 ultramicrotome. Fourier transform infrared (FT-IR) measurement was carried out on a Varian Digilab FTS-8010 spectrophotometer. PeakForce Quantitative Nanomechanical Mapping (PFQNM) characterizations of surface elastic modulus were measured by Multimode 8. AFM-IR measurements were obtained from a Bruker Anasys nanoIR3 system. Simultaneous acquisition of topographic and chemical images by tapping mode. The HRTEM images were captured on a JEM-2100F transmission electron microscope. A UV2501-PC spectrophotometer was used to get Ultraviolet-visible (UV-vis) absorption spectra. Two-dimensional (2D) glancing incidence experiments were performed at the Xeuss3.0. Dielectric constants and dissipation factors were measured using an Alpha-A High Performance Frequency Analyzer, and the samples (diameter 3.4 mm and thickness about 30-40 μm) were deposited on a 30 nm thick copper. The polarization-electric field (P-E) loops were collected using a Polarization Loop & Dielectric Breakdown Test System from PolyK, where AC electric fields with an increment of 10 MV m^{-1} were applied across polymer films with a triangular waveform at a frequency of 1 Hz and 10 Hz. Leakage current density was acquired from a Keithley Model 6517 A electrometer equipped with a Trek Model 610 C amplifier. Thermally stimulated depolarization current (TSDC) was measured by a Keithley 6517 A electrometer. The samples were firstly polarized under 20 MV m^{-1} at 40 °C for 20 minutes a Trek Model 610 C amplifier. Then the temperature was quickly dropped to -10 °C with the electric field on. After that, the samples were disconnected from the electric field and short-circuited for 2 minutes. Finally, the samples were heated from -10 °C to 60 °C at a rate of 1 °C min^{-1} and the current was recorded. Differential scanning calorimetry (DSC) data was collected by a DSC Q2000 with a heating rate of 10 °C min^{-1}. High-speed camera images and movies were captured by the SONY DSC-RX10III digital camera. High voltage was provided by a high-voltage power supply (Dongwen, DW-P103-0). The electrostrictive strain (thickness deformation) of the films was measured using a non-contact photonic sensor system (MTI-2100 Fotonic Sensor, 2032 R probe). As illustrated in Supplementary Fig. S36, the sample was placed between parallel plate electrodes, and the thickness change was measured perpendicularly by the probe. The reported strain values were recorded at 0.1 s or 1 s after field application to ensure the capture of steady-state response.

Data availability

The data generated in this study are provided in the Supplementary Information/Source Data file. All data are available from the corresponding author upon request. Source data are provided with this paper.

References

1. Aubin, C. A. et al. Powerful, soft combustion actuators for insect-scale robots. *Science* **381**, 1212–1217 (2023).
2. Goldberg, B. et al. Power and control autonomy for high-speed locomotion with an insect-scale legged robot. *IEEE Robot. Autom. Let.* **3**, 987–993 (2018).
3. Ji, X. et al. An autonomous untethered fast soft robotic insect driven by low-voltage dielectric elastomer actuators. *Sci. Robot.* **4**, eaaz6451 (2019).
4. Yang, X., Chang, L. & Pérez-Arancibia, N. O. An 88-milligram insect-scale autonomous crawling robot driven by a catalytic artificial muscle. *Sci. Robot.* **5**, eaba0015 (2020).
5. Kurniawan, R. et al. in *2020 IEEE/RSJ International Conference on Intelligent Robots and Systems (IROS)*, 7881–7886 (2020).
6. Noh, M., Kim, S. W., An, S., Koh, J. S. & Cho, K. J. Flea-inspired catapult mechanism for miniature jumping robots. *IEEE T. Robot.* **28**, 1007–1018 (2012).
7. Koh, J.-S. et al. Jumping on water: Surface tension–dominated jumping of water striders and robotic insects. *Science* **349**, 517–521 (2015).
8. Kovac, M., Fuchs, M., Guignard, A., Zufferey, J. C. & Floreano, D. in *2008 IEEE International Conference on Robotics and Automation*, 373–378 (2008).
9. Jafferis, N. T., Helbling, E. F., Karpelson, M. & Wood, R. J. Untethered flight of an insect-sized flapping-wing microscale aerial vehicle. *Nature* **570**, 491–495 (2019).
10. Ren, Z. et al. A high-lift micro-aerial-robot powered by low-voltage and long-endurance dielectric elastomer actuators. *Adv. Mater.* **34**, 2106757 (2022).
11. Choe, K. et al. Performance characteristics of electro–chemically driven polyacrylonitrile fiber bundle actuators. *J. Intel. Mat. Syst. Str.* **17**, 563–576 (2006).
12. Suzumori, K., Iikura, S. & Tanaka, H. Applying a flexible microactuator to robotic mechanisms. *IEEE Contr. Syst. Mag.* **12**, (1992).
13. Loomis, J., Xu, P. & Panchapakesan, B. Stimuli-responsive transformation in carbon nanotube/expanding microsphere–polymer composites. *Nanotechnology* **24**, 185703 (2013).
14. Cheng, N. G., Gopinath, A., Wang, L., Iagnemma, K. & Hosoi, A. E. Thermally tunable, self-healing composites for soft robotic applications. *Macromol. Mater. Eng.* **299**, 1279–1284 (2014).
15. Carpi, F., Bauer, S. & De Rossi, D. Stretching dielectric elastomer performance. *Science* **330**, 1759–1761 (2010).
16. Sadeghipour, K., Salomon, R. & Neogi, S. Development of a novel electrochemically active membrane and 'smart' material based vibration sensor/damper. *Smart Mater. Struct.* **1**, 172 (1992).
17. Chen, Y. et al. Controlled flight of a microrobot powered by soft artificial muscles. *Nature* **575**, 324–329 (2019).
18. Youn, J.-H. et al. Dielectric elastomer actuator for soft robotics applications and challenges. *Appl. Sci.* **10**, 640 (2020).
19. Mei, D. et al. A soft crawling robot with multi-modal locomotion inspired by the movement mechanism of snake scales. *IEEE Robot. Autom. Let.* **9**, 7589–7596 (2024).
20. Chen, X. et al. Relaxor ferroelectric polymer exhibits ultrahigh electromechanical coupling at low electric field. *Science* **375**, 1418–1422 (2022).
21. Zhang, Z., Wang, X., Tan, S. & Wang, Q. Superior electrostrictive strain achieved under low electric fields in relaxor ferroelectric polymers. *J. Mater. Chem. A* **7**, 5201–5208 (2019).
22. Park, S.-E. & Shrout, T. R. Ultrahigh strain and piezoelectric behavior in relaxor based ferroelectric single crystals. *J. Appl. Phys.* **82**, 1804–1811 (1997).
23. Shi, Y. et al. A processable, high-performance dielectric elastomer and multilayering process. *Science* **377**, 228–232 (2022).
24. Zhu, S. et al. Highly photoluminescent carbon dots for multicolor patterning, sensors, and bioimaging. *Angew. Chem. Int. Ed.* **52**, 3953–3957 (2013).
25. Chinaglia, D. L. et al. Influence of the solvent evaporation rate on the crystalline phases of solution-cast poly(vinylidene fluoride) films. *J. Appl. Polym. Sci.* **116**, 785–791 (2010).
26. Song, R. et al. Enhanced β phase of polyvinylidene fluoride with addition of polyamide 6: role of interfacial interactions. *Colloid Polym. Sci.* **292**, 817–828 (2014).
27. Su, Y. et al. High-performance piezoelectric composites via β phase programming. *Nat. Commun.* **13**, 4867 (2022).
28. Liu, Y. et al. Chirality-induced relaxor properties in ferroelectric polymers. *Nat. Mater.* **19**, 1169–1174 (2020).
29. Xu, H. et al. Ferroelectric and electromechanical properties of poly(vinylidene-fluoride–trifluoroethylene–chlorotrifluoroethylene) terpolymer. *Appl. Phys. Lett.* **78**, 2360–2362 (2001).
30. Zhang, Q. M., Bharti, V. & Zhao, X. Giant electrostriction and relaxor ferroelectric behavior in electron-irradiated poly(vinylidene fluoride-trifluoroethylene) copolymer. *Science* **280**, 2101–2104 (1998).
31. Zhang, Q. M. et al. An all-organic composite actuator material with a high dielectric constant. *Nature* **419**, 284–287 (2002).
32. Cross, L. E. Ferroelectric ceramics: materials and application issues. *Ceram. Trans.* **68**, 15–55 (1996).
33. Trolier-McKinstry, S., Zhang, S., Bell, A. J. & Tan, X. High-performance piezoelectric crystals, ceramics, and films. *Annu. Rev. Mater. Res.* **48**, 191–217 (2018).
34. Ma, K. Y., Chirarattananon, P., Fuller, S. B. & Wood, R. J. Controlled flight of a biologically inspired, insect-scale robot. *Science* **340**, 603–607 (2013).
35. Li, T. et al. Fast-moving soft electronic fish. *Sci. Adv.* **3**, e1602045 (2017).
36. Christianson, C. et al. Jellyfish-inspired soft robot driven by fluid electrode dielectric organic robotic actuators. *Front. Robot. AI* **6**, 126 (2019).
37. Wu, Y. et al. Insect-scale fast moving and ultrarobust soft robot. *Sci. Robot.* **4**, eaax1594 (2019).
38. Shintake, J., Cacucciolo, V., Shea, H. & Floreano, D. Soft biomimetic fish robot made of dielectric elastomer actuators. *Soft Robot* **5**, 466–474 (2018).
39. Gu, G., Zou, J., Zhao, R., Zhao, X. & Zhu, X. Soft wall-climbing robots. *Sci. Robot.* **3**, eaat2874 (2018).
40. Chen, Y., Xu, S., Ren, Z. & Chirarattananon, P. Collision resilient insect-scale soft-actuated aerial robots with high agility. *IEEE T. Robot.* **37**, 1752–1764 (2021).
41. Duduta, M. et al. Electrically-latched compliant jumping mechanism based on a dielectric elastomer actuator. *Smart Mater. Struct.* **28**, 09LT01 (2019).
42. Cao, J. et al. Untethered soft robot capable of stable locomotion using soft electrostatic actuators. *Extrem. Mech. Lett.* **21**, 9–16 (2018).

Acknowledgements

This research was funded by the Jilin Province Science and Technology Development Programs of China (No. 20240602002RC), the National Natural Science Fund of China (52473215, 52273248, and 52303238) and Key Project of Natural Science Foundation of Tianjin City (S24JQU021 and QN20230102).

Author contributions

Y.H.Z., R.J.M., and H.C. conceived and designed the research. H.C. and P.J.B. prepared the samples. H.C., P.J.B., and Z.X.Z. conducted the electrical and electromechanical measurements. H.C. and W.H.X. collected the XRD and FTIR data. H.C. performed the dielectric measurements. H.C. and G.F.W. performed the AFM-IR measurements. H.C.

performed the strain measurements. H.C., P.J.B., and X.R.W. prepared the bionic actuators and conducted actuation tests. H.C. carried out the transmission electron microscopy measurements. Y.Z. and H.Q. performed PFQNM characterizations of surface elastic modulus. H.C. and W.H.X. wrote the manuscript with input from all authors. Y.H.Z., R.J.M., and W.H.X. supervised the research.

Competing interests

The authors declare no competing interests.

Additional information

Supplementary information The online version contains supplementary material available at https://doi.org/10.1038/s41467-026-70165-0.

Correspondence and requests for materials should be addressed to Wenhan Xu, Yunhe Zhang or Rujun Ma.

Peer review information *Nature Communications* thanks Zhicheng Zhang and the other anonymous reviewer(s) for their contribution to the peer review of this work. A peer review file is available.

Reprints and permissions information is available at http://www.nature.com/reprints

Publisher's note Springer Nature remains neutral with regard to jurisdictional claims in published maps and institutional affiliations.

Open Access This article is licensed under a Creative Commons Attribution-NonCommercial-NoDerivatives 4.0 International License, which permits any non-commercial use, sharing, distribution and reproduction in any medium or format, as long as you give appropriate credit to the original author(s) and the source, provide a link to the Creative Commons licence, and indicate if you modified the licensed material. You do not have permission under this licence to share adapted material derived from this article or parts of it. The images or other third party material in this article are included in the article's Creative Commons licence, unless indicated otherwise in a credit line to the material. If material is not included in the article's Creative Commons licence and your intended use is not permitted by statutory regulation or exceeds the permitted use, you will need to obtain permission directly from the copyright holder. To view a copy of this licence, visit http://creativecommons.org/licenses/by-nc-nd/4.0/.

© The Author(s) 2026